

Supporting Information Materials for

Synergistic effect by supported activated carbon between functional groups and metal oxygen vacancies: Enhancing Ibuprofen degradation by improving ozone mass transfer

Junda Lai ^a, Zizheng Huangfu ^a, Jiewen Xiao ^a, Zhenbei Wang ^a, Yatao Liu ^a, Chen Li ^a, Fan Li ^a, Yunhan Jia ^a, Qiang Wang ^a, Fei Qi ^{a*}, Amir Ikhlaq ^b, Jolanta Kumirska ^c, Ewa Maria Siedlecka ^c, Oksana Ismailova ^{d, e}

^a Beijing Key Lab for Source Control Technology of Water Pollution, College of Environmental Science and Engineering, Beijing Forestry University, Beijing 100083, PR China

^b Institute of Environment Engineering and Research, University of Engineering and Technology, GT Road, 54890 Lahore, Punjab, Pakistan.

^c Department of Environmental Analysis, Faculty of Chemistry, University of Gdansk, Wita Stwosza 63, 80-308, Poland.

^d Uzbekistan-Japan Innovation Center of Youth, Tashkent State Technical University, Tashkent 100095, Uzbekistan

^e Turin Polytechnic University Tashkent, Tashkent 100095, Uzbekistan

* Corresponding author: Prof. Fei Qi

Tel.: +86 10 62336615; Fax: +86 10 62336596

Email address: qifei@bjfu.edu.cn; qifei_hit@163.com (Fei. Qi)

List of Captions

Text S1 The samples pretreatment methodology and specific conditions for characterization.

Text S2 Catalytic ozonation and decomposition experiments.

Text S3 Analytical methods.

Text S4 Quantitative analysis of formed ROS.

Text S5 The calculation methods for energy consumption and ozone utilization efficiency.

Text S6 Binding energy calculation.

Text S7 Load optimization of $\text{CuMn}_2\text{O}_4@\text{WAC}$ and $\text{CuMn}_2\text{O}_4@\text{CSAC}$.

Text S8 The economic analysis of $\text{CuMn}_2\text{O}_4@\text{WAC}$ and $\text{CuMn}_2\text{O}_4@\text{CSAC}$.

Text S9 Calculation of ozone mass transfer parameters.

Text S10 The XRD patterns of $\text{CuMn}_2\text{O}_4@\text{WAC}$ and $\text{CuMn}_2\text{O}_4@\text{CSAC}$.

Text S11 The N_2 adsorption-desorption isotherms.

Text S12 The SEM images.

Text S13 The EDS results.

Text S14 The XPS full survey spectrum of ACs.

Table S1 Reaction rate constant of ozone molecule and hydroxyl radical with IBP, AMX, CIP, CBZ.

Table S2 Removal efficiency of typical refractory organics by catalytic ozonation reported by literature.

Table S3 The water quality parameters of the secondary effluent of pharmaceutical wastewater.

Table S4 Catalyst cost and operating expenses.

Table S5 Metal ions leaching in catalytic ozonation and the effect of the operation time on this.

Table S6 Metal ions leaching in catalytic ozonation in the presence of solid catalyst reported in the published literature.

Table S7 Related parameters in Mass transfer of ozone in the sole ozonation or catalytic ozonation.

Table S8 Specific surface area and pore size of studied activated carbon and its supported catalyst.

Table S9 Analysis of elemental content of activated carbon and its supported catalyst.

Table S10 Elemental composition of activated carbon and supported catalyst.

Table S11 Relative amount of Cu/Mn of activated carbon supported catalyst obtained from XPS energy spectrum.

Table S12 Relative amount of potential active components in activated carbon and its supported catalyst obtained from XPS energy spectrum.

Table S13 The related content of MeO-D hydrogen bond observed by ATR-FITR of the catalyst surface w/o the molecule ozone.

Table S14 Relative amount of the surface chemical functional group of activated carbon supported catalyst.

Fig. S1. Synthesis schematic of CuMn_2O_4 and $\text{MnO}_2\text{-Co}_3\text{O}_4$ supported catalysts.

Fig. S2 Schematic diagram of the catalytic ozonation experiments installation.

Fig. S3 IBP removal efficiency (a), mineralization (b), obtained k_{obs} value (min^{-1}) (c) and TOC removal efficiency (d) by catalytic ozonation.

Fig. S4 Removal efficiency of IBP (a), AMX (b), CIP (c), CBZ (d) by supported catalysts, performance (e) and cost analysis (f) in catalytic ozonation.

Fig. S5 Removal efficiency and mineralization of IBP by catalytic ozonation of WAC (a, b); CSAC (c, d) under different elemental contents.

Fig. S6 Evolution of ozone utilization efficiency (a) and energy consumption (EEC) (b) in IBP degradation by catalytic ozonation.

Fig. S7 Removal efficiency of IBP (a), AMX (b), CIP (c), CBZ (d) by catalytic ozonation by supported catalysts in the secondary effluent of pharmaceutical wastewater.

Fig. S8 The reusability evaluation of $\text{CuMn}_2\text{O}_4@\text{WAC}$ (a, b) and $\text{CuMn}_2\text{O}_4@\text{CSAC}$ (c, d).

Fig. S9 The effect of ozone concentration on ozone dissolution (a) and ozone dissolution dynamics (b); effect of ozone concentration on the ozone decomposition in deionized water (c) and ozone decomposition kinetics (d).

Fig. S10 XRD spectrum of $\text{CuMn}_2\text{O}_4@\text{WAC}$ (a) and $\text{CuMn}_2\text{O}_4@\text{CSAC}$ (b) activated carbon adsorption and desorption isotherm of N_2 gas (c).

Fig. S11 Relationship between surface adsorption and observed reaction rate constant (k_{obs}) (a); Specific surface (b) and micropore volume (c) on k_{obs} in IBP degradation in the presence of AC or AC supported CuMn_2O_4 .

Fig. S12 SEM images of WAC (a) $\text{CuMn}_2\text{O}_4@\text{WAC}$ (b) CSAC (c) and $\text{CuMn}_2\text{O}_4@\text{CSAC}$ (d).

Fig. S13 EDS spectrum of WAC (a) $\text{CuMn}_2\text{O}_4@WAC$ (b) CSAC (c) and $\text{CuMn}_2\text{O}_4@CSAC$ (d).

Fig. S14 XPS full spectrum of activated carbon and activated carbon supported CuMn_2O_4 (a) and XPS spectra of activated carbon-supported CuMn_2O_4 : (b) C 1s, (c) Mn 2p, (d) Cu 2p (e).

Fig. S15 The geometry structure of (a) pristine crystal plane (311), Mn- O_v plane (b) and Cu- O_v plane (c).

Fig. S16 Reaction mechanism of activated carbon supported CuMn_2O_4 catalytic ozonation of refractory organics in wastewater.

Text S1 The samples pretreatment methodology and specific conditions for characterization.

The crystal phase of the sample was identified using an X-ray diffractometer (XRD-7000, Shimadzu, Japan). In this case, a Cu/K α X-ray source with a wavelength (λ) of 0.154 nm was used. The tube voltage was set at 40 kV and the tube current at 30 mA. The scanning speed was 4°/min, with a step width of 0.02°, covering a scanning range (2θ) from 5° to 85°.

Scanning electron microscopy-energy dispersive X-ray spectroscopy (SEM-EDS; SU8000, Hitachi, Japan) was employed to observe the microscopic morphology and determine the element content of the samples. The operating conditions were as follows: the accelerating voltage was set to 5.0 kV, the current was 5.0 μ A, and the working distance between the sample and the catalyst was 8.0 mm. Prior to sample measurement, the catalyst was sputter-coated with ion beam deposition for 80 s.

Attenuated total reflection fourier transform infrared spectroscopy (ATR-FTIR; Vertex 70, Bruker, Germany) was utilized to characterize the surface chemical functional groups of the samples. The blank experiment was conducted under a nitrogen atmosphere by adding catalyst (0.1 g) and D₂O (2 mL) to centrifuge tube (5 mL), followed by sonication for 5 minutes. The solid was separated by centrifugation and treated again with D₂O (2 mL) to eliminate residual water. The sample was immediately sealed and centrifuged, with half of the supernatant used as a control and the other half suspended as the sample. During the interaction between the catalyst

and ozone, after removing residual water from the solid sample, Ozone (30 mg/L) was bubbled into the centrifuge tube under initial conditions of pH 7. The sample was immediately sealed and centrifuged. The solid concentration during this process was 100 g/L. Infrared spectra in the range of 4000-650 cm^{-1} were obtained at room temperature through 32 scans, with a resolution of 4 cm^{-1} .

X-ray photoelectron spectroscopy (XPS; AXIS Ultra, Kratos Analysis Co., Ltd.) was used to analyze the chemical bonding state and valence of the elements in the MFB before and after reaction, where the instrument is equipped with hemispherical electron analysis and Mg $K\alpha$ ($h\nu = 1253.6$ eV) X-ray source. The C 1s peak (248.6 eV) of the samples was used as the internal standard to correct the electron binding energy (B. E.) value.

The surface oxygen species of the catalyst were analyzed using Raman spectroscopy (inVia-reflex, Renishaw). 0.1 g catalyst powder (0.1 g) was mixed with water (3mL) in two separate groups: one group without ozone (blank) and the other group exposed to ozone (experimental group). Sample (0.5 mL) was extracted and placed into reaction cell for analysis. The Raman spectrometer utilized a laser with wavelength of 532 nm, scanning the samples from 400 cm^{-1} to 1200 cm^{-1} with resolution of 1 cm^{-1} and acquisition time of 30 s.

Text S2 Catalytic ozonation and decomposition experiments.

The cylindrical glass reactor used for the experiments had a diameter of 4.0 cm and a height of 22.0 cm, resulting in an effective solution volume of 276.0 mL. To generate ozone, an ozone generator (3S-A5, Tonglin China) was utilized, and the ozone concentration in the gas phase was measured using an ozone analyzer (GM-6000-OEM, Anshan Ansiros Environmental Protection Co., Ltd, Anshan, China). To ensure a stable ozone gas concentration, the ozone generator was operated for 30 min before the catalytic ozonation process.

Initially, an IBP solution with a concentration of 13.1 mg/L in 200 mL was added to the reactor, followed by the introduction of a specific mass of particle catalyst. Subsequently, ozone was continuously supplied to the reactor through a microporous aeration plate at a flow rate of 100 mL/min. The initiation of the reaction occurred upon the introduction of ozone.

At specified time intervals, samples were extracted from the reactor and immediately quenched using Na_2SO_3 (0.1 mM). These samples were then filtered through a 0.45 μm filter, which exhibited no adsorption of IBP and total organic carbon (TOC). The concentrations of IBP and TOC were subsequently determined separately. It is important to highlight that in this study, IBP was exclusively used as a probe to assess the performance of the proposed catalysts. The predetermined concentration of IBP, contributing to 9.9 mg/L TOC, was chosen to simulate the water quality of secondary effluent in a typical pharmaceutical wastewater treatment process.

By using the secondary effluent from the pharmaceutical wastewater treatment process as the matrix, the IBP concentration decreased to 1.0 mg/L, thus simulating the pharmaceutical wastewater.

The experiment was conducted in the aforementioned reactor using a similar ozone input procedure as described earlier. The only difference was that IBP was not added. After achieving a stable dissolved ozone concentration in ultrapure deionized water, the ozone generator was switched off. Samples were then collected at specific time intervals and passed through a 0.45 μm filter. These filtered samples were used to determine the dissolved ozone concentration using the indigo method^{1, 2}. Firstly, the absorbance of the ozone-free water sample was measured at 612 nm using UV-visible spectrophotometer. The absorbance of the sample obtained after dilution was denoted as A_0 . Next, the absorbance of the sample containing dissolved ozone was measured. Specifically, the sample (1.0 mL), along with the indigo disulfonate sodium solution (1.0 mL, 0.5 g/L) and the phosphate buffer solution (5.0 mL), were added to colorimetric tube (25 mL) and diluted with deionized water. The absorbance of the resulting sample, which represented A_1 , was measured. Finally, the concentration of dissolved ozone (C_{O_3}) was calculated using Eq. (S1).

$$C_{O_3} = (A_1 - A_0) \times 60 \quad (\text{S1})$$

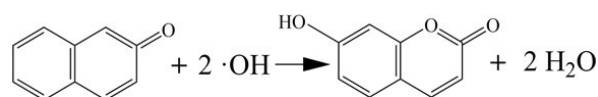
Text S3 Analytical methods.

The concentration of IBP in water was measured using an HPLC (Waters-2695, Waters Corporation, USA) system equipped with a UV detector (Waters-2998, Waters Corporation, USA) operating at a wavelength of 612 nm. The chromatographic separation was performed using a C18 column (Agilent Corporation, USA). To determine the residual total organic carbon (TOC) in the solution, a TOC analyzer employing differential subtraction was utilized. This analysis involved maintaining an oxygen pressure of 200 Pa and an oxygen gas flow rate of 130 mL/min.

COU, Amplex red, and NBD-Cl were utilized as probe molecules to measure the concentrations of hydroxyl radicals ($\bullet\text{OH}$), hydrogen peroxide (H_2O_2), and superoxide radicals ($\bullet\text{O}_2^-$) formed, respectively³⁻⁵. The fluorescence intensity was detected by recording the fluorescence emission spectrum using a fluorescence spectrophotometer (F-7000, Hitachi, Japan). The corresponding detailed procedures for the above analyses were described in Text S7 of the respective studies. Furthermore, the concentration of dissolved metal ions was determined using an atomic absorption spectrophotometer (AA-6880F, Shimadzu, Japan).

Text S4 Quantitative analysis of formed ROS.

The use of coumarin (COU) as a probe was employed to measure the concentration of hydroxyl radicals ($[\bullet\text{OH}]$), which resulted in the production of fluorescent 7-hydroxycoumarin (7-HC) through COU's selective reaction with $\bullet\text{OH}$, as depicted in Eq. (S2). Specifically, a 200 mL solution of coumarin with a concentration of 20 mg/L was introduced into the reactor. At specific intervals, samples were taken from the reactor and treated with Na_2SO_3 solution (10.0 mM), then filtered using a vial through a 0.22 μm PTFE filter that did not impact the final analysis. [7-HC] concentration was quantified using a fluorescence spectrometer (F-7000, Hitachi, Japan) with excitation at 332 nm and detection of 7-HC's fluorescence intensity at 455 nm, with the slits set to 5.0 nm³.



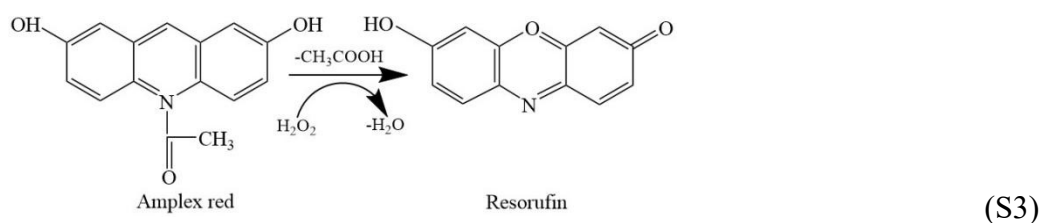
Coumarin (COU)

7-hydroxycoumarin (7-HC)

(S2)

To determine the concentration of superoxide radicals ($[\bullet\text{O}_2^-]$), a probe called 4-chloro-7-nitrobenzofurazan (NBD-Cl) was selected, which resulted in the formation of a fluorescent product through the reaction between $\bullet\text{O}_2^-$ and NBD-Cl. The fluorescence intensity of this product was measured by recording the emission spectrum using a fluorescence spectrometer (F-7000, Hitachi, Japan), with excitation at 470 nm. The formation of the NBD-Cl product was confirmed by reacting NBD-Cl with KO_2 , which served as a source of superoxide ions. The amount of superoxide ion radicals was quantified by plotting the fluorescence at 550 nm against the

concentration of $\bullet\text{O}_2^-$ using a fixed concentration of 20 mg/L NBD-Cl and varying concentrations of KO_2 . Prior to analysis on the fluorescence spectrometer, all aqueous samples (1 mL) were mixed with acetonitrile (2 mL). Amplex red, an effective probe in aqueous of H_2O_2 , selectively reacted with H_2O_2 (Eq. (S3)) to form fluorescent Resorufin that was able to be detected by fluorescence spectrometer (F-7000, Hitachi, Japan). In detail, after pre-purge with ozone, IBP were then added into the solution simultaneously to acquire the required concentrations. At certain time intervals, samples (1 mL) were withdrawn from the reactor and immediately added into 3.0 mL Amplex red solution (20 mg/L), reacting for 30 min and then analyzed with F-7000 Fluorescence Spectrometer at 587 nm (excited at 563 nm). Both the emission and excitation slits were set to 5.0 nm.



Text S5 The calculation methods for energy consumption and ozone utilization efficiency.

$$EEC = \frac{P * Q_{O_3} \int [O_3]_{in} dt}{1000 * V * \log \frac{c_0}{c_t}} \quad (S4)$$

where, $[O_3]_{in}$ is the gaseous O_3 concentration in the inlet, V is the volume (as 0.2 L in study). P is the energy required to generate O_3 through the ozone generator, (32 kWh/kg O_3); t is the sampling time (min).

$$OUE = \frac{\int_0^t [Q_{(O_3)} ([O_3]_{in} - [O_3]_{out})] dt - V [O_3]_{dissolve}}{\int_0^t Q_{(O_3)} [O_3]_{in} dt} \quad (S5)$$

where, $[O_3]_{in}$ is the gaseous O_3 concentration in the inlet and $[O_3]_{out}$ is the gaseous O_3 concentration in outlet, Q_{O_3} is the gas flow (as 100 mL/min in study); V is the volume (as 0.2 L in study). P is the energy required to generate O_3 through the ozone generator, (32 kWh/kg O_3); t is the sampling time (min).

Text S6 Binding energy calculation.

The model calculates the adsorption energy of molecular ozone according to Eq. (S6), where E_{total} , $E_{surface}$, and E_{O_3} refer to total energy of whole system, the pure surface, and energy for O_3 molecule. The charge density is calculated using Eq. (S7).

$$\Delta E_b = E_{total} - E_{surface} - E_{O_3} \quad (S6)$$

$$\Delta \rho = \rho_{O_3/surface} - \rho_{O_3} - \rho_{surface} \quad (S7)$$

Where, $\rho_{O_3/surface}$, ρ_{O_3} , and $\rho_{surface}$ are the charge densities of the configuration after

O₃ is adsorbed on the surface.

Text S7 Load optimization of CuMn₂O₄@WAC and CuMn₂O₄@CSAC.

In order to get best performance, the active component loading amount was optimized and results were shown in Fig. S4(a)-(b). When the loading amounts of Mn and Cu were 1.5 wt.% and 0.73 wt.%, respectively, the removal efficiency of IBP and TOC were 98.7% and 64% in catalytic ozonation by CuMn₂O₄@WAC, respectively. Increasing the loading amounts to 6.0 wt.% and 2.92 wt.%, resulted in higher removal efficiency of IBP (99.9%) and TOC (84%). However, further increasing the loading amounts to 12.0 wt.% of Mn and 5.84 wt.% of Cu, did not lead to significant development on the removal efficiency of IBP and TOC. Therefore, it was determined that the optimal loading amount was 6.0 wt.% of Mn and 2.92 wt.% of Cu by using CuMn₂O₄@WAC in catalytic ozonation.

When using CuMn₂O₄@CSAC in catalytic ozonation, the best loading of active component was optimized as 6.0 wt.% Mn and 2.92 wt.% Cu (Fig. S4(c)-(d)). When the loading was less than this, the removal efficiency of IBP and TOC increased to 99.9% and 82%, respectively, when the loading amount increased. When the loading increased to 12.0 wt.% Mn and 5.84 wt.% Cu, the performance did not improved well for both the removal efficiency of IBP and TOC.

Increasing the loading amount enhances the content of active sites on the catalyst's surface, thereby improving the catalytic ability of ozone decomposition and accelerating this process, further increasing the production of •OH (Eqs. (S8)-(S11)). On the other hand, when the loading amount continues to increase, it may cause aggregation of catalyst particles, reducing the contact area between ozone and the active sites on the catalyst's surface, thereby inhibiting the formation of •OH and impeding the degradation of IBP.





Text S8 The economic analysis of CuMn₂O₄@WAC and CuMn₂O₄@CSAC.

The economic analysis of this study considers the costs associated with preparing CuMn₂O₄@WAC and CuMn₂O₄@CSAC catalysts, including raw material expenses, reagent costs, and electricity fees, as well as the production costs of ozone, primarily involving industrial oxygen and electricity consumption. Furthermore, taking into account the catalysts' reusability and estimated lifespan contributes to a more comprehensive assessment of the economic benefits and sustainability of the entire wastewater treatment process. These cost and benefit analyses are crucial for devising effective wastewater treatment strategies and resource management, ensuring the economic efficiency and environmental friendliness of the treatment process.

The cost of ozone production mainly includes the raw material cost of oxygen and electricity consumption. Calculated at an industrial oxygen price of 1000 CNY/ton, producing 1 ton of ozone requires 12000 CNY for the cost of oxygen. Based on the parameters of the ozone generator using oxygen as the gas source, the electricity consumption of the ozone generator ranges from 6 to 10 kWh/kg O₃. Calculated at an industrial electricity price of 0.5 CNY/kWh, the cost of ozone production is 5000 CNY/ton, resulting in a total unit cost of 17000 CNY/ton. The cost of preparing

CuMn₂O₄@WAC and CuMn₂O₄@CSAC catalysts includes raw materials and electricity expenses. The required materials for preparing 1 ton of CuMn₂O₄@WAC and CuMn₂O₄@CSAC catalysts include WAC (6000 CNY/ton), CSAC (10000 CNY/ton), copper nitrate, manganese nitrate dihydrate, oxalic acid, etc., with electricity costs calculated at 640 CNY/ton. The catalysts are reusable, with an estimated lifespan of approximately 534 hours. The required catalyst dosage for treating 1 ton of pharmaceutical wastewater is 0.42 kg/ton. The ozone required for degrading unit COD can be found in Eq. S12. The detailed standard cost of treating 1 ton of water using a combination of ozone and catalytic oxidation processes is presented in Table S4.

$$\text{Ozone consumption (kg/kg COD)} = \frac{t \times Q_{O_3} \times [O_3]_{in} \times 10^{-6}}{V \times (C_0 - C_t) \times 10^{-6}} \quad (\text{S12})$$

Where t represents the reaction time, which is 90 minutes in this study; Q_{O_3} stands for the flow rate of gaseous ozone, which is 0.1 L/min in this study; $[O_3]_{in}$ indicates the concentration of gaseous ozone at the inlet, which is 5 mg/L in this study; V represents the volume of the reaction solution, which is 0.2 L in this study; C_0 denotes the initial COD (mg/L), and C_t represents the COD at time t (mg/L).

Text S9 Calculation of ozone mass transfer parameters.

There is a Eq. S13 according to the mass balance of dissolved ozone within the reactor.

$$\frac{d[O_3]}{dt} = K_{La} ([O_3]^* - [O_3]_{ss}) - K_d [O_3] \quad (S13)$$

Where k_{La} is the overall volume mass transfer coefficient (min^{-1}), k_d is rate constant (min^{-1}) of the O_3 decomposition, $[O_3]^*$ is the concentration (mg/L) of saturated dissolved ozone, $[O_3]_{ss}$ is the concentration of steady-state ozone (mg/L), and $[O_3]$ is the actual concentration of dissolved ozone in the liquid phase (mg/L) over a defined time.

When the concentration of solute reaches a stable state, cumulative term $\frac{d[O_3]}{dt}$ is tends to Eq. (S13) is transformed into Eq. (S14).

$$K_d C_{ss} = K_{La} ([O_3]^* - [O_3]_{ss}) \quad (S14)$$

Since the reaction liquid film is controlled, the interfacial concentration $[O_3]$ is equal to $[O_3]^*$, $[O_3]^*$ is the concentration (mg/L) of saturated dissolved ozone in water under certain conditions. Eq. (S13) and Eq. (S14) are respectively converted to Eq. (S15) and Eq. (S16), respectively.

$$\frac{d[O_3]}{dt} = K_{La} ([O_3]^* - [O_3]) - K_d [O_3] \quad (S15)$$

$$K_d C_{ss} = K_{La} ([O_3]^* - [O_3]_{ss}) \quad (S16)$$

And then, Eq. (S17) is obtained by deforming from Eq. (S16).

$$[O_3]_{ss} = \frac{[O_3]}{1 + \frac{K_d}{K_{La}}} \quad (S17)$$

Combining the Eq. (S16) and Eq. (S17) to obtained Eq. (S18) and Eq. (S19).

$$\frac{d[O_3]}{dt} = K_{La} \left(\frac{[O_3]_{ss} (K_{La} + K_d)}{K_{La}} - [O_3] \right) - K_d [O_3] \quad (S18)$$

$$\frac{d[O_3]}{dt} = ([O_{ss}] - [O_3]) (K_{La} + K_d) \quad (S19)$$

Integrating both sides of the equation, and when the initial condition is $[O_3]=0$ mg/L, Eq. (S20) and Eq. (21) are obtained.

$$\int \frac{1}{[O_{ss}] - [O_3]} d[O_3] = \int (K_{La} + K_d) dt \quad (S20)$$

$$\ln \frac{[O_3]_{ss}}{[O_3]_{ss} - [O_3]} = -(K_{La} + K_d)t \quad (S21)$$

$k_{La}+k_d$ can be used as a slope for linear regression fitting, subtracting the value of the k_d to give k_{La} . When the conveying of O_3 is stopped, Eq. (S15) transformed to Eq. (S22).

$$\frac{d[O_3]}{dt} = -K_d [O_3] \quad (S22)$$

Integrating Eq. (S22), with the initial condition $[O_3]=0$ mg/L, Eqs. (S23) and (S24) were gotten.

$$\int \frac{1}{[O_3]} d[O_3] = \int K_d dt \quad (S23)$$

$$\ln \frac{[O_3]_{ss}}{[O_3]} = K_d t \quad (S24)$$

Text S10 The XRD patterns of $\text{CuMn}_2\text{O}_4@\text{WAC}$ and $\text{CuMn}_2\text{O}_4@\text{CSAC}$.

Two distinct diffraction peaks appeared at 23.7° and 43.7° on the surfaces of WAC and CSAC, respectively, indicating that both ACs have amorphous carbon structures⁶. The characteristic peaks of CuMn_2O_4 (JCPDS 42-1169) were observed at 28.9° , 37.4° , and 56.8° on the surfaces of both WAC and CSAC, indicating successful loading of CuMn_2O_4 onto the activated carbons.

Text S11 The N_2 adsorption-desorption isotherms.

The N_2 adsorption-desorption isotherms of the four ACs showed type I isotherms, indicating that they were microporous materials. The adsorption capacity of the four ACs decreased in the order of $\text{CBAC} > \text{WAC} > \text{CSAC} > \text{FSAC}$. The ranking of ACs adsorption capacity was generally consistent with its adsorption characteristics for IBP, as well as its catalytic properties in the decomposition of IBP, the relationship between AC adsorption and catalysis can be seen in Fig. S10(a).

Text S12 The SEM images.

The SEM images in Fig. S11(a) showed that surface of WAC had a large number of pores, which was beneficial for the loading of metal oxides. After being loaded with CuMn_2O_4 (as shown in Fig. S11(b)), the surface and pores of the WAC were blocked by nanoscale particles, resulting in the appearance of agglomerated particles on its surface. Before being loaded (as shown in Fig. S11(c)), CSAC had fewer pores. After being loaded with CuMn_2O_4 (as shown in Fig. S11(d)), the surface of the CSAC became rough and uneven, with increased surface pores and the appearance of numerous irregular agglomerated particles.

Text S13 The EDS results.

Furthermore, the EDS results (Fig. S12(a)) indicated that the surface of WAC had an even distribution of oxygen (19.73%) and carbon (80.27%) elements. After loading with CuMn_2O_4 , Mn and Cu elements appeared on the surface of WAC (Fig. S12(b)). The contents of Mn and Cu on the surface of $\text{CuMn}_2\text{O}_4@\text{WAC}$ was 4.57% and 2.11%, respectively (Table S9). As shown in Table S9, the surface of CSAC also exhibited an even distribution of O (19.73%) and C (80.27%) elements, respectively. After loading with CuMn_2O_4 , the contents of Mn and Cu on the surface of $\text{CuMn}_2\text{O}_4@\text{CSAC}$ were 4.17% and 2.15%, respectively. Additionally, the atomic ratios of Mn/Cu on $\text{CuMn}_2\text{O}_4@\text{WAC}$ and $\text{CuMn}_2\text{O}_4@\text{CSAC}$ were 2.1 and 1.9, respectively, which was closed to the theoretical value of $\text{CuMn}_2\text{O}_4@\text{WAC}$ and $\text{CuMn}_2\text{O}_4@\text{CSAC}$.

Text S14 The XPS full survey spectrum of ACs.

Fig. S13(a) presented the XPS full survey spectrum of the four types of AC. The main elements detected in all AC samples were C and O. However, after loading with CuMn_2O_4 , characteristic peaks attributed to Mn and Cu elements also appeared on the surface of both WAC and CSAC, alongside C and O elements. Table S10 provided the compositions of WAC, CSAC, $\text{CuMn}_2\text{O}_4@\text{WAC}$, and $\text{CuMn}_2\text{O}_4@\text{CSAC}$. The content of Mn and Cu elements on $\text{CuMn}_2\text{O}_4@\text{WAC}$ was 0.42% and 0.19%, respectively, with a Mn (at.):Cu (at.) ratio of 2.2 (theoretical value = 2). Similarly, on $\text{CuMn}_2\text{O}_4@\text{CSAC}$, the content of Mn and Cu elements was 0.62% and 0.32%, respectively, and the Mn (at.):Cu (at.) ratio was 1.9 (theoretical value = 2) (Table S10).

**Table S1 Reaction rate constant of ozone molecule and hydroxyl radical with
IBP, AMX, CIP, CBZ.**

Compound	Molecular formula	Ozone molecule k (L/ (mol·s))	Ref.	Hydroxyl radical k (L/ (mol·s))	Ref.
IBP	$C_{18}H_{13}O_2$	7.2	7	9.6×10^9	8
AMX	$C_{16}H_{19}N_3O_5S$	7×10^6	9	2.02×10^9	2
CIP	$C_{17}H_{18}O$	2×10^5	10	6.2×10^9	11
CBZ	$C_{15}H_{15}N_2O$	3×10^5	12	2.1×10^9	13

Table S2 Removal efficiency of typical refractory organics by catalytic ozonation reported by literature.

Compounds	Catalyst	Operating conditions	k_{obs} (min ⁻¹)	$k_{obs, normalize}$ (per mg/L pollutant concentration)	EEO (kWh/m ³)	k_{La} (min ⁻¹)	Ref.
Humic Acid	Fe/Zeolite	V=2 L O ₃ gas flow = 1.0 L/min [O ₃] _{in} = 10 mg/L HA = 30 mg/L catalyst dosage = 0.75 g/L t=30 min	0.16	0.0053	32.0	-----	14
Humic Acid	Fe/MgO	V=2.5 L O ₃ gas flow = 2.35 L/min	0.15	0.003	2.6	-----	15

		[O ₃] _{in} = 17.8 mg/L					
		HA = 50 mg/L					
		catalyst dosage = 10 g/L					
		t=60 min					
		V=2000 L					
		O ₃ gas flow = 3.0 L/min					
Coal	Fe-Mn@	[O ₃] _{in} = 88.5 mg/L	0.01	0.000003	11.0	-----	16
gasification	Lava rocks	COD = 3200 mg/L					
wastewater		catalyst dosage = 40 g/L					
		t=120 min					
		V=1 L					
Sulfanilamide	CeO _x @SiO ₂	O ₃ gas flow = 1.0 L/min	0.17	0.017	-----	0.451	17

$[O_3]_{in} = 0.8 \text{ mg/L}$

sulfanilamide = 10 mg/L

catalyst dosage = 0.2 g/L

t=120 min

O_3 gas flow = 1 L/min

$Q_L = 1 \text{ L/min}$

Nitrobenzene	Cu-MnO _x / γ - Al ₂ O ₃	$[O_3]_{in} = 75 \text{ mg/L}$ Nitrobenzene =125 mg/L catalyst dosage = 15 g/L t=40 min	0.19	0.0015	9.0	-----	18
Pyridine	MnxCu1- xOy/ γ -Al ₂ O ₃	O_3 gas flow = 1.0 L/min, V=1 L	0.03	0.00011	33.6	-----	19

		[O ₃] _{in} = 35 mg/L					
		pyridine = 270 mg/L					
		catalyst dosage = 340 g/L					
		t=60 min					
		O ₃ gas flow = 1.0 L/min,					
NO adding		V=2 L					
target organic	Fe - Mn -	[O ₃] _{in} = 60 mg/L	-----	-----	-----	0.696	20
probe	Cu/ γ -Al ₂ O ₃	catalyst dosage = 340 g/L					
		t=10 min					
	Mn-	O ₃ gas flow =0.02 L/min					
Ciprofloxacin	CeOx@ γ -	V=0.6 L	0.57	0.0114	6.4	0.626	21
	Al ₂ O ₃	[O ₃] _{in} =14 mg/L					

		CIP=50 mg/L					
		catalyst dosage = 80 g/L					
		t=100 min					
		O ₃ gas flow =3 L/min					
		V=3 L					
Acid Red B	Fe-Co@foam	[O ₃] _{in} =20 mg/L	0.158	0.00026	-----	0.400	22
	block	ARB=600 mg/L					
		catalyst dosage = 80 g/L					
		t=12 min					
		O ₃ gas flow =0.1 L/min					
Ibuprofen	CuMn ₂ O ₄ @	V=0.2 L	0.113	0.0086	0.80	0.381	This work
	WAC	[O ₃] _{in} =5 mg/L					

IBP=13.1 mg/L

catalyst dosage = 125 g/L

t=60 min

O₃ gas flow =0.1 L/min

V=0.2 L

Ibuprofen	CuMn ₂ O ₄ @	[O ₃] _{in} =14 mg/L	0.093	0.0071	1.11	0.362	This work
	CSAC	IBP=13.1 mg/L					
		catalyst dosage = 125 g/L					
		t=60 min					

Table S3 The water quality parameters of the secondary effluent of pharmaceutical wastewater.

COD (mg/L)	SS (mg/L)	TN (mg/L)	NH ₃ -N (mg/L)	pH	TDS (mg/L)
100.00	67.00	36.85	13.35	8.23	4233.00

Table S4 Catalyst cost and operating expenses.

Process Type	Ozone Consumption (kg/kg COD)	Ozone Cost (CNY/kg COD)	Catalyst Dosage (kg/ton)	Catalyst Cost (CNY/ton)	Ozone Cost (CNY/ton water)	Catalyst Cost (CNY/ton water)	Total Cost (CNY/ton water)
Ozonation	12.50	212.5	0	0	21.25	0	21.25
Ozonation by CuMn ₂ O ₄ @WAC	5.63	95.7	0.42	10886	9.57	4.30	13.87
Ozonation by CuMn ₂ O ₄ @CSAC	6.82	115.9	0.42	14886	11.59	5.98	17.57

Table S5 Metal ions leaching in catalytic ozonation and the effect of the operation time on this.

Times of catalyst uses	Time (min)	CuMn ₂ O ₄ @WAC		CuMn ₂ O ₄ @CSAC	
		T[Mn] (mg/L)	T[Cu] (mg/L)	T[Mn] (mg/L)	T[Cu] (mg/L)
1	5	0.19	0.72	0.49	0.67
	30	0.17	0.71	0.45	0.63
	60	0.14	0.64	0.39	0.63
	90	0.16	0.62	0.41	0.64
	120	0.17	0.80	0.35	0.63
2	5	0.14	0.71	0.35	0.66
	30	0.15	0.68	0.30	0.65
	60	0.20	0.64	0.45	0.64
	90	0.19	0.63	0.42	0.63
	120	0.27	0.63	0.36	0.66
3	5	0.47	0.98	0.35	0.65
	30	0.39	0.62	0.44	0.64
	60	0.25	0.63	0.50	0.72
	90	0.20	0.61	0.47	0.66
	120	0.41	0.65	0.58	0.72
4	5	0.20	0.62	0.58	0.81

Times of catalyst uses	Time (min)	CuMn ₂ O ₄ @WAC		CuMn ₂ O ₄ @CSAC	
		T[Mn] (mg/L)	T[Cu] (mg/L)	T[Mn] (mg/L)	T[Cu] (mg/L)
	30	0.22	0.61	0.53	0.80
	60	0.27	0.61	0.55	0.74
	90	0.24	0.61	0.47	0.66
	120	0.57	0.66	0.58	0.66
	5	0.20	0.71	0.47	0.72
	30	0.22	0.68	0.49	0.66
5	60	0.27	0.64	0.55	0.64
	90	0.24	0.63	0.56	0.72
	120	0.57	0.63	0.58	0.66

Experiment condition: ozone dosage=5 mg/L, gas flow rate =100 mL/min, volume=200 mL,

catalyst particles packed rate =10%.

Table S6 Metal ions leaching in catalytic ozonation in the presence of solid catalyst reported in the published literature.

Catalyst	Operating conditions	Loading (g/kg)	Leaching (mg/L)	Solubility ratio (%)	Ref.
Mn-CeOx@ γ -Al ₂ O ₃	V=1 L				
	pH=6.3				
	catalyst dosage =	[Mn]=35.1	[Mn]=0.39	Mn=0.014	23
	80 g/L	[Ce]=53.4	[Ce]=0.16	Ce=0.037	
	t=120 min				
CuO/SiO ₂	V=0.2 L				
	pH=3				
	catalyst dosage =	[Cu]=30	[Cu]=0.30	Mn=0.20	24
	5 g/L				
	t=30 min				
Ag ₂ O/SiO ₂	V=0.2 L				
	pH=3				
	catalyst dosage =	[Ag]=36	[Ag]=7.0	Ag=3.8	24
	5 g/L				
	t=30 min				
Cu@hydrotalcite	V=0.4 L				
	pH=3	[Cu]=81	[Cu]=50	Cu=6.17	25

	catalyst dosage =				
	10 g/L				
	t=30 min				
	V=1 L				
	pH=9				
Fe-		[Fe]=82	[Fe]=2.30	Fe=0.023	
Ni/MAC	catalyst dosage =	[Ni]=67	[Ni]=3.50	Ni=0.050	26
	10 g/L				
	t=90 min				
	V=0.5 L				
	pH=3				
Ce-Ti-		[Ce]=121	[Ce]=0.04	Ce=0.007	
Zr@SA	catalyst dosage =				27
	5 g/L				
	t=120 min				
	V=0.5 L				
	pH=3				
Pt/Al ₂ O ₃	catalyst dosage =	[Pt]=10	[Pt]=10	Al =0.050	28
	10 g/L				
	t=120 min				
	V=0.5 L				
Fe/Al ₂ O ₃	catalyst dosage =	[Fe]=87	[Fe]=0.05	[Fe]=0.05	29
	1 g/L				

t=120 min					
V=0.5 L					
Ni/Al ₂ O ₃	catalyst dosage = 1 g/L	[Ni]=128	[Ni]=2.00	[Ni]=1.0	30
t=120 min					
V=0.5 L					
Cu/Al ₂ O ₃	catalyst dosage = 1 g/L	[Cu]=35	[Cu]=5.2	[Cu]=14.85	30
t=120 min					
V=0.2 L					
CuMn ₂ O ₄	pH=6.3	[Mn]=10.8	[Mn]=0.44	Mn=0.03	This work
@WAC	catalyst dosage = 125 g/L	[Cu]=5.3	[Cu]=0.18	Cu=0.027	
t=120 min					
V=0.2 L					
CuMn ₂ O ₄	pH=6.3	[Mn]=4.5	[Mn]=0.24	Mn=0.042	This work
@CSAC	catalyst dosage = 125 g/L	[Cu]=12.3	[Cu]=0.63	Cu=0.041	
t=120 min					

Table S7 Related parameters in Mass transfer of ozone in the sole ozonation or catalytic ozonation.

Reaction type	Ozone dosage (mg/L)	Support or Supporting Catalyst	(K_d+K_{La}) (min ⁻¹)	K_d (min ⁻¹)	K_{La} (min ⁻¹)
Sole ozonation	5	-----	0.272	0.091	0.181
Catalytic ozonation	5	WAC	0.886	0.532	0.354
Catalytic ozonation	5	CSAC	0.807	0.491	0.316
Catalytic ozonation	5	CuMn ₂ O ₄ @WAC	0.919	0.538	0.381
Catalytic ozonation	5	CuMn ₂ O ₄ @CSAC	0.920	0.558	0.362

Table S8 Specific surface area and pore size of studied activated carbon and its supported catalyst.

Sample name	Specific surface area (m ² /g)	Total pore volume (cm ³ /g)	Micropore volume (cm ³ /g)	Average pore size (nm)
CBAC	995.811	0.498	0.353	3.823
WAC	872.652	0.367	0.328	3.810
CSAC	718.662	0.305	0.263	3.821
FSAC	245.202	0.126	0.080	3.410
CuMn ₂ O ₄ @WAC	793.617	0.332	0.293	3.801
CuMn ₂ O ₄ @CSAC	717.601	0.303	0.261	3.189

Table S9 Analysis of elemental content of activated carbon and its supported catalyst.

Element	WAC (wt.%)	CSAC (wt.%)	CuMn ₂ O ₄ @WAC (wt.%)	CuMn ₂ O ₄ @CSAC (wt.%)
O	19.73	21.73	17.21	18.45
C	80.27	78.28	76.11	75.25
Mn	----	-----	4.57	4.17
Cu	----	-----	2.11	2.15

Table S10 Elemental composition of activated carbon and supported catalyst.

Catalyst	C (at. %)	O (at. %)	Mn (at. %)	Cu (at. %)
CBAC	92.31	7.69	---	---
WAC	90.26	9.74	---	---
CSAC	92.49	7.51	---	---
FSAC	84.82	15.18	---	---
CuMn ₂ O ₄ @WAC	87.80	11.77	0.42	0.19
CuMn ₂ O ₄ @CSAC	92.02	7.21	0.62	0.32

Table S11 Relative amount of Cu/Mn of activated carbon supported catalyst obtained from XPS energy spectrum.

Sample name	Mn ³⁺ /Mn ⁴⁺	Cu ⁺ /Cu ²⁺	Mn/Cu
CuMn ₂ O ₄ @WAC	2.12	0.87	2.2 (theory 2)
CuMn ₂ O ₄ @CSAC	1.77	0.27	1.9 (theory 2)

Table S12 Relative amount of potencial active components in activated carbon and its supported catalyst obtained from XPS energy spectrum.

Sample name	C=C/C-C	-C-O-C-	-C=O	O-C=O
	content (%)	content (%)	content (%)	content (%)
CBAC	63.35	15.70	10.77	10.18
WAC	63.78	12.78	11.74	8.70
CSAC	64.90	13.02	13.09	8.99
FSAC	62.80	24.02	10.69	2.49
CuMn ₂ O ₄ @WAC	61.34	21.37	11.07	6.22
CuMn ₂ O ₄ @CSAC	62.12	22.37	10.39	5.12

Table S13 The related content of MeO-D hydrogen bond observed by ATR-FITR of the catalyst surface w/o the molecule ozone.

Sample name	Peak area	
	Before reaction	After reaction
WAC	29.77	35.26
CSAC	30.09	38.18
CuMn ₂ O ₄ @WAC	44.74	73.99
CuMn ₂ O ₄ @CSAC	46.27	75.84

Table S14 Relative amount of the surface chemical functional group of activated carbon supported catalyst.

Sample name	Carboxyl group (mmol/g)	Lactone group (mmol/g)	Phenolic hydroxyl group (mmol/g)
CBAC	1.5633	0.07125	0.075
WAC	1.175	0.15	0.2
CSAC	1.425	0.05	0.225
FSAC	0.7	0.1	0.175
CuMn ₂ O ₄ @WAC	0.8	0.01	0.0375
CuMn ₂ O ₄ @CSAC	0.725	0.025	0.075

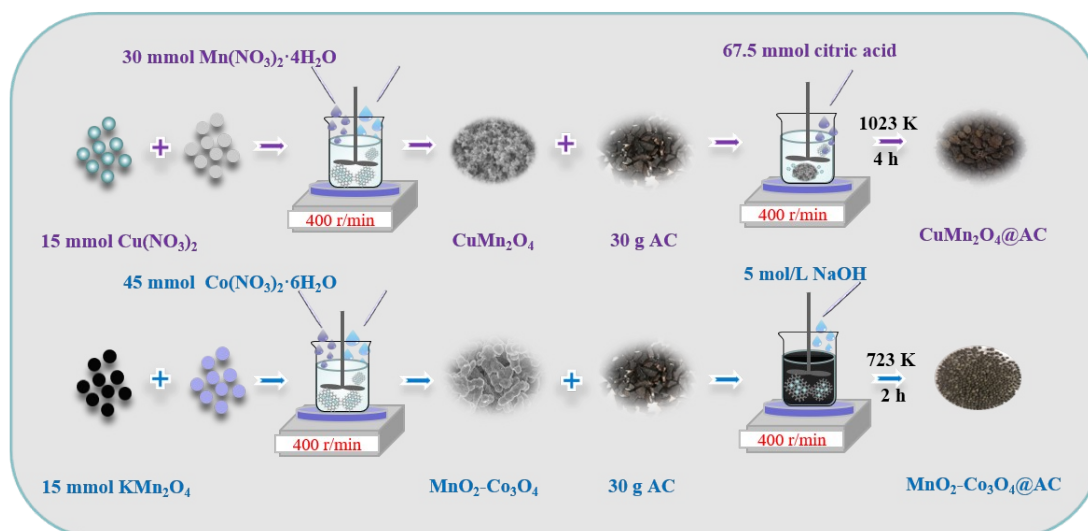


Fig. S1. Synthesis schematic of CuMn_2O_4 and $\text{MnO}_2\text{-Co}_3\text{O}_4$ supported catalysts

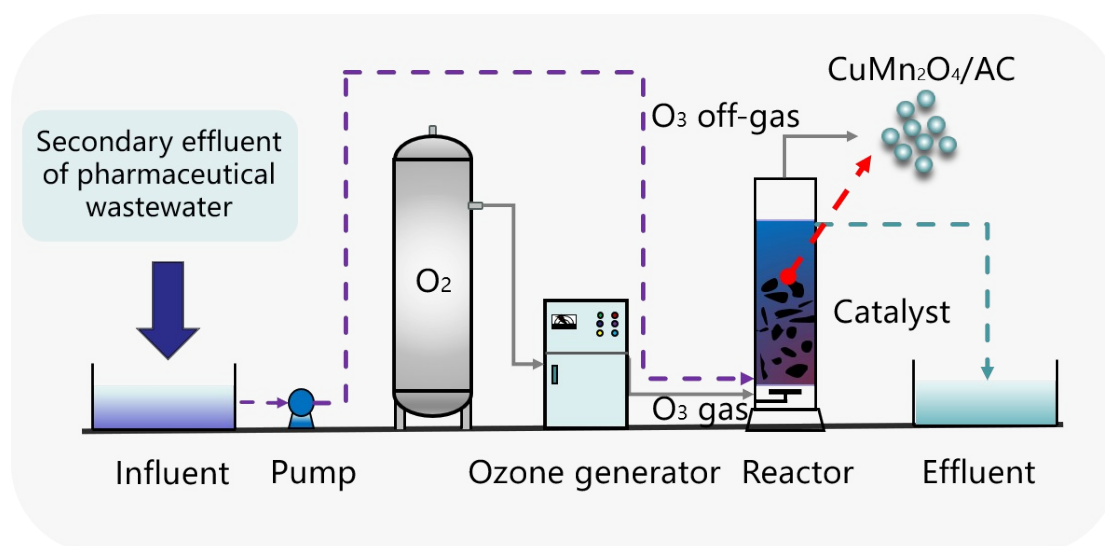


Fig. S2 Schematic diagram of the catalytic ozonation experiments installation.

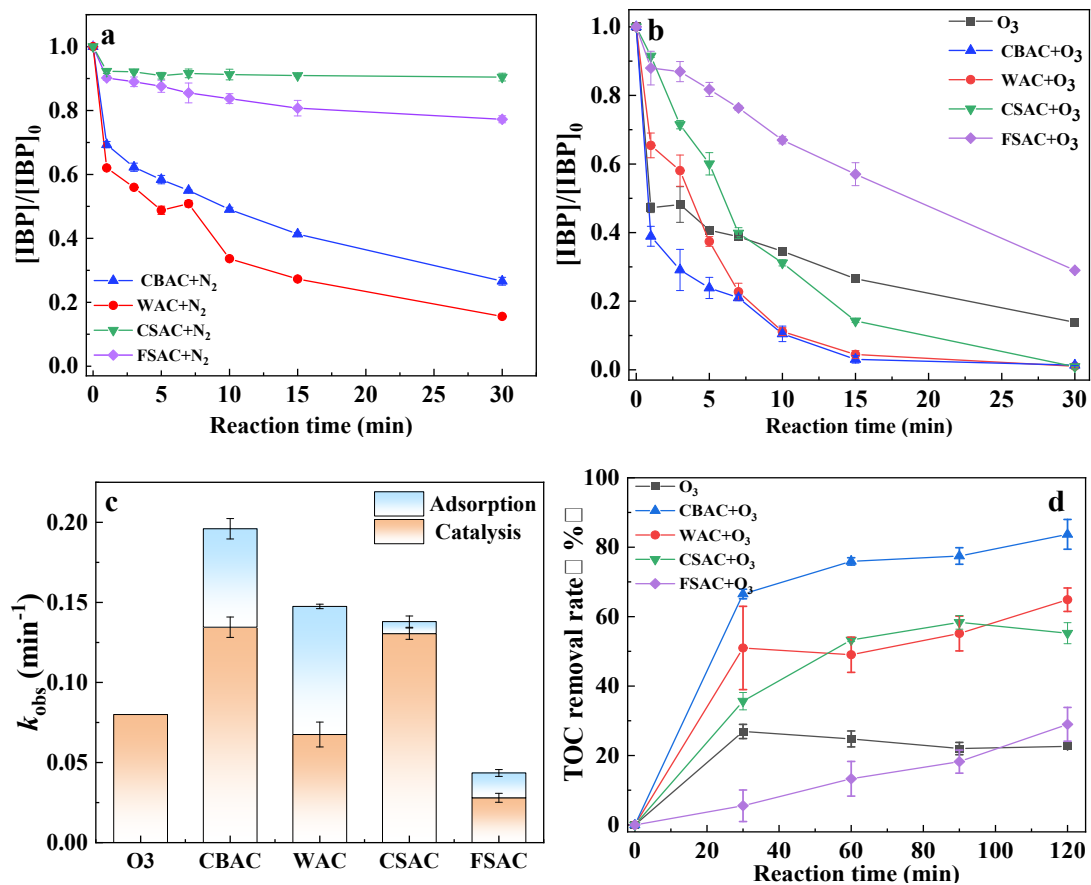


Fig. S3 IBP removal efficiency (a), mineralization (b), obtained k_{obs} value (min^{-1}) (c) and TOC removal efficiency (d) by catalytic ozonation. Experimental conditions: $[\text{IBP}] = 13.1 \text{ mg/L}$, ozone dosage = 5 mg/L , gas flow rate = 100 mL/min , volume = 200 mL , catalyst particles packed rate = 10% .

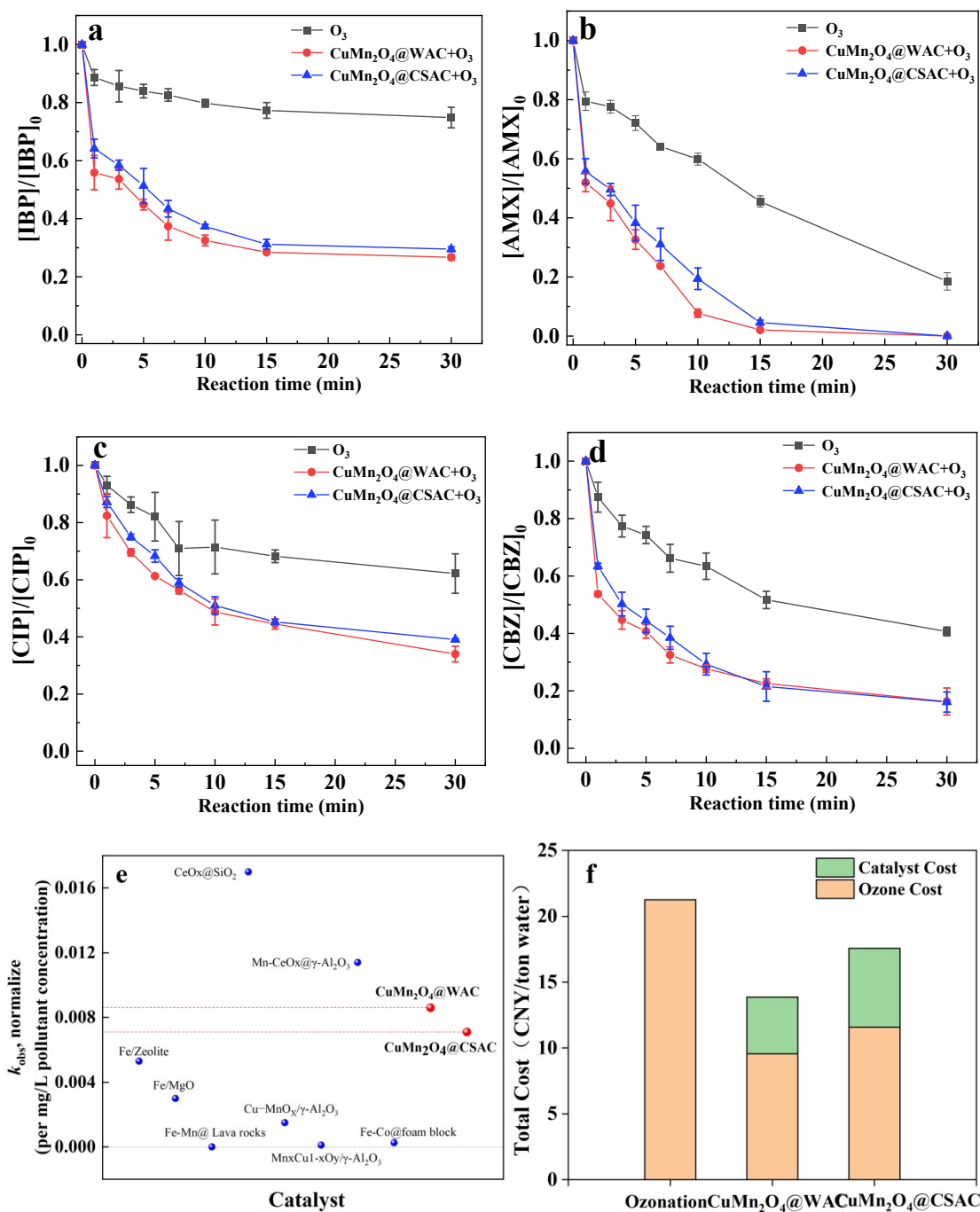


Fig. S4 Removal efficiency of IBP (a), AMX (b), CIP (c), CBZ (d) by supported catalysts, performance (e) and cost analysis (f) in catalytic ozonation. Experimental conditions: $[IBP]=[AMX]=[CIP]=[CBZ]=0.065$ mol/L, ozone dosage =5 mg/L, gas flow rate =100 mL/min, volume=200 mL, catalyst particles packed rate =10%.

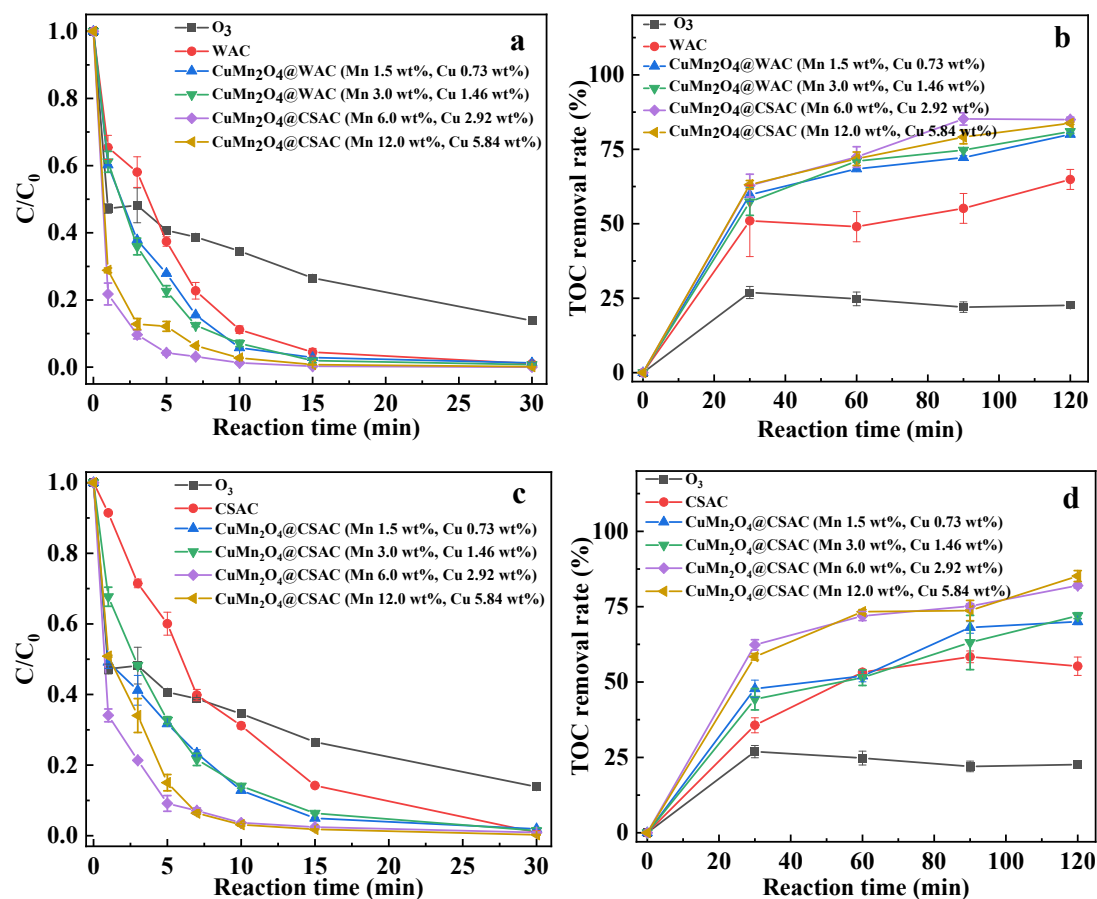


Fig. S5 Removal efficiency and mineralization of IBP by catalytic ozonation of WAC (a, b); CSAC (c, d) under different elemental contents. Experimental conditions: [IBP]=13.1 mg/L, ozone dosage =5 mg/L, gas flow rate =100 mL/min, volume=200 mL, catalyst particles packed rate =10%.

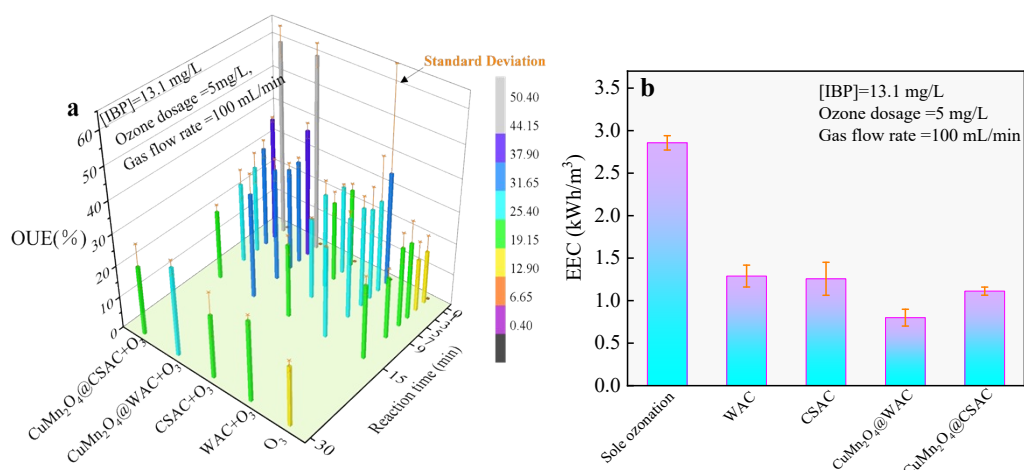


Fig. S6 Evolution of ozone utilization efficiency (a) and energy consumption (EEC) (b) in IBP degradation by catalytic ozonation. Experimental conditions: [IBP]=13.1 mg/L, ozone dosage =5 mg/L, gas flow rate =100 mL/min, reaction volume=200 mL, catalyst particles packed rate =10%.

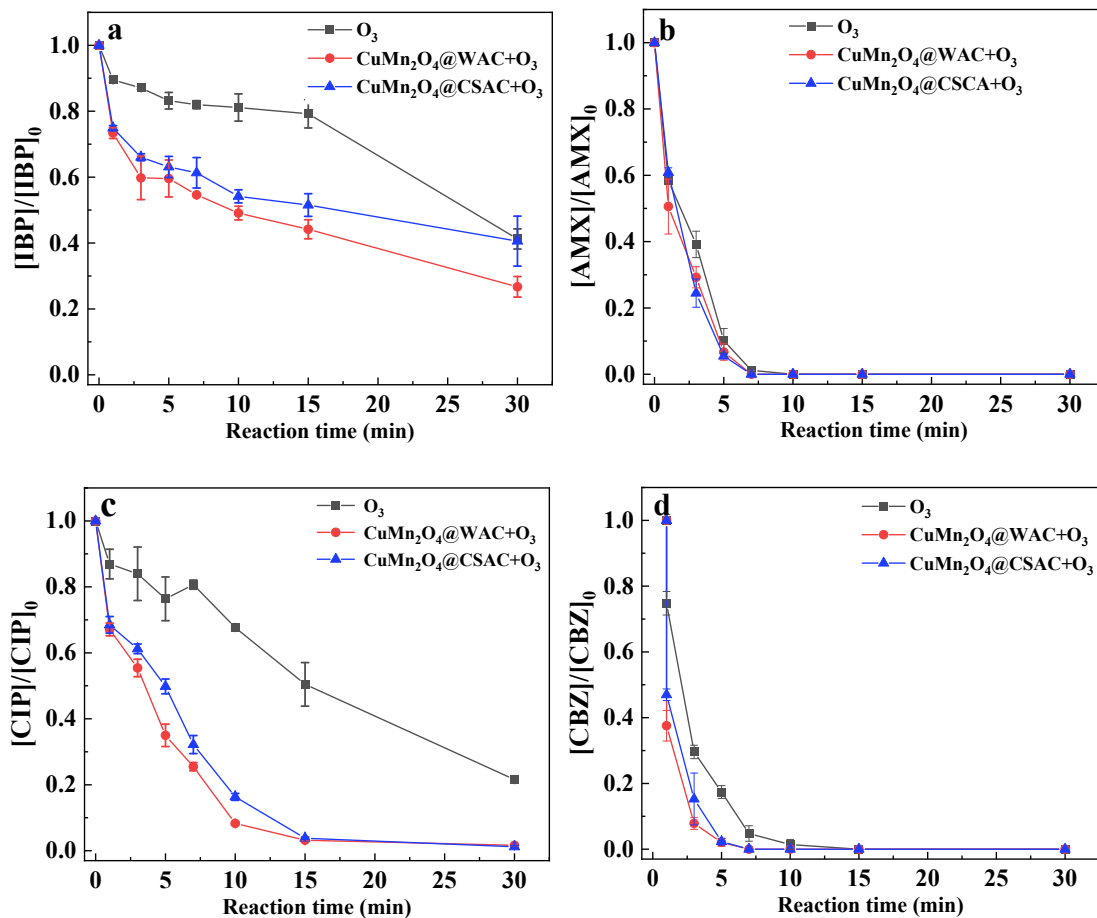


Fig. S7 Removal efficiency of IBP (a), AMX (b), CIP (c), CBZ (d) by catalytic ozonation by supported catalysts in the secondary effluent of pharmaceutical wastewater. Experimental conditions: $[IBP]=[AMX]=[CIP]=[CBZ]=0.0065$ mol/L, ozone dosage = 5 mg/L, gas flow rate = 100 mL/min, volume = 200 mL, catalyst particles packed rate = 10%.

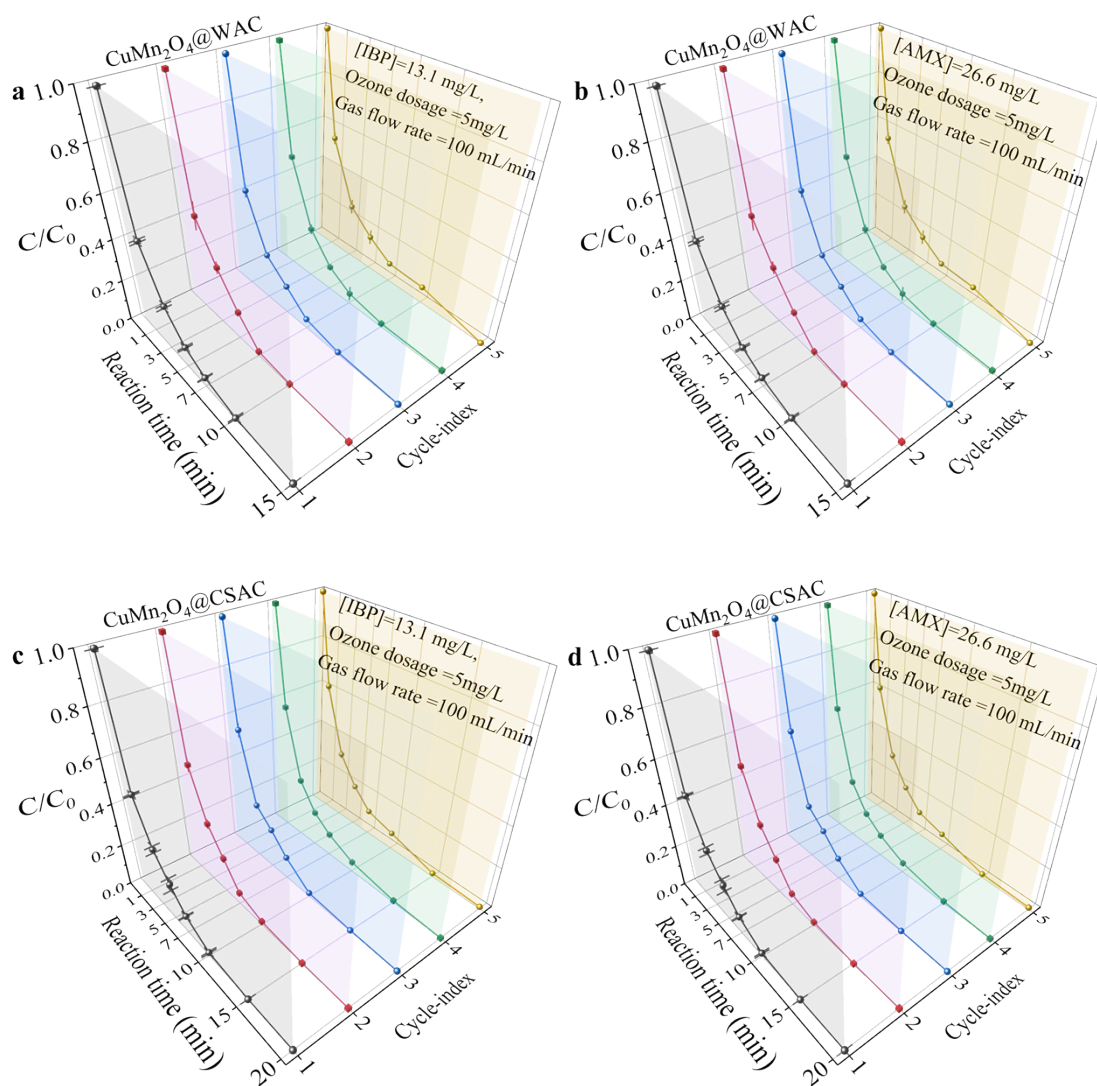


Fig. S8 The reusability evaluation of CuMn_2O_4 @WAC (a, b) and CuMn_2O_4 @CSAC (c, d). Experimental conditions: [IBP]=13.1 mg/L, [AMX]=26.6 mg/L, ozone dosage = 5 mg/L, gas flow rate = 100 mL/min, volume = 200 mL, catalyst particles packed rate = 10%.

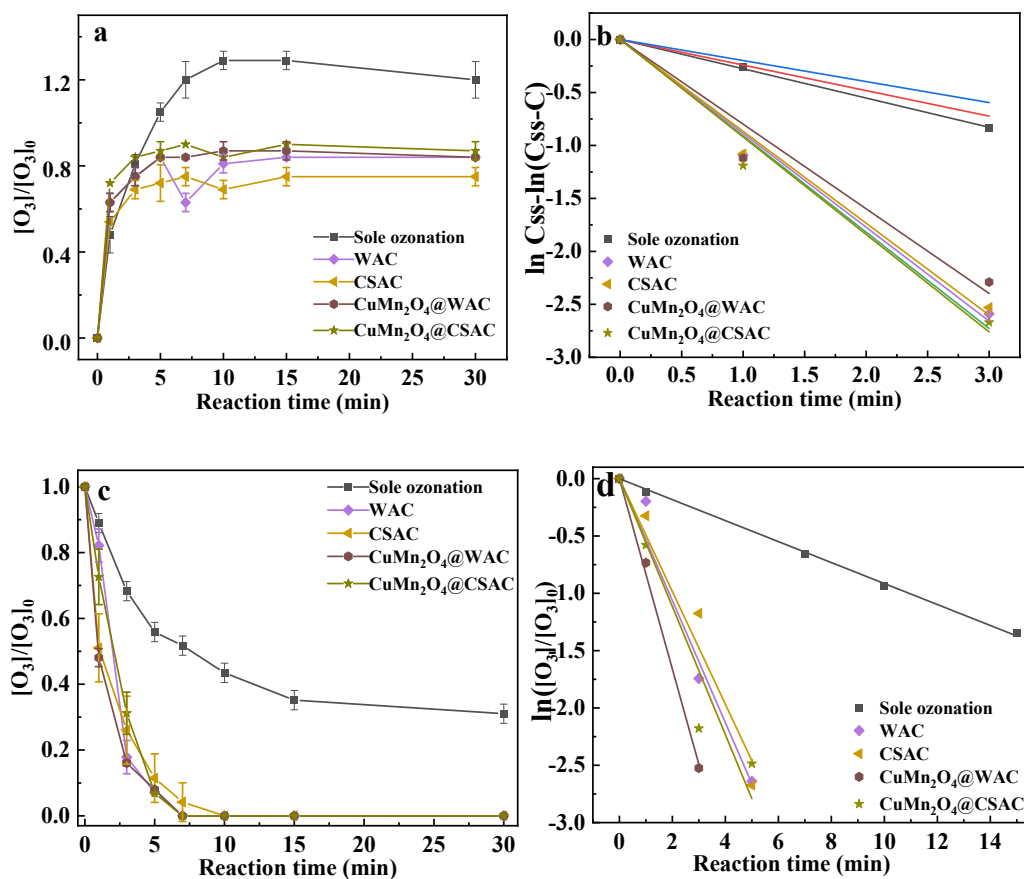


Fig. S9 The effect of ozone concentration on ozone dissolution (a) and ozone dissolution dynamics (b); effect of ozone concentration on the ozone decomposition in deionized water (c) and ozone decomposition kinetics (d).

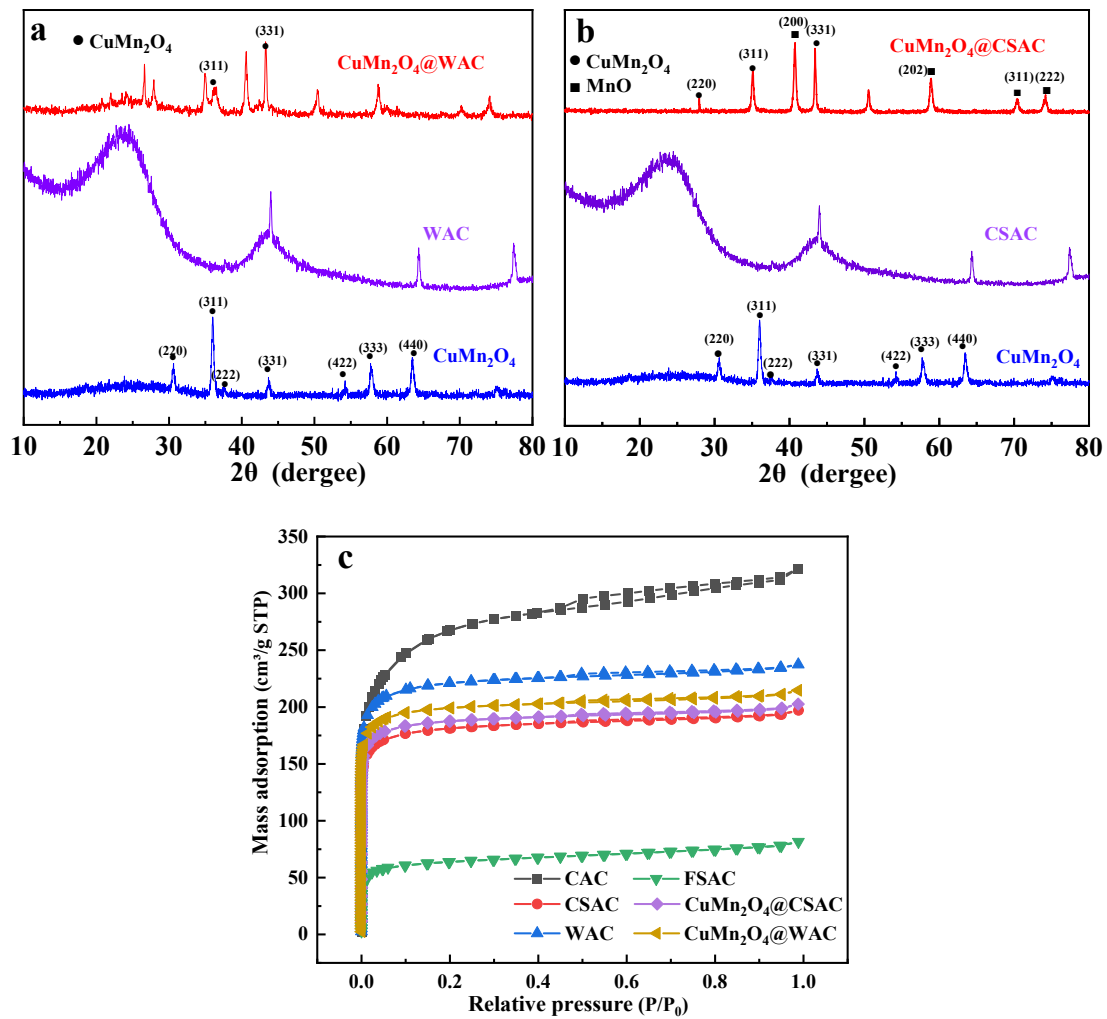


Fig. S10 XRD spectrum of $\text{CuMn}_2\text{O}_4@WAC$ (a) and $\text{CuMn}_2\text{O}_4@CSAC$ (b) activated carbon adsorption and desorption isotherm of N_2 gas (c).

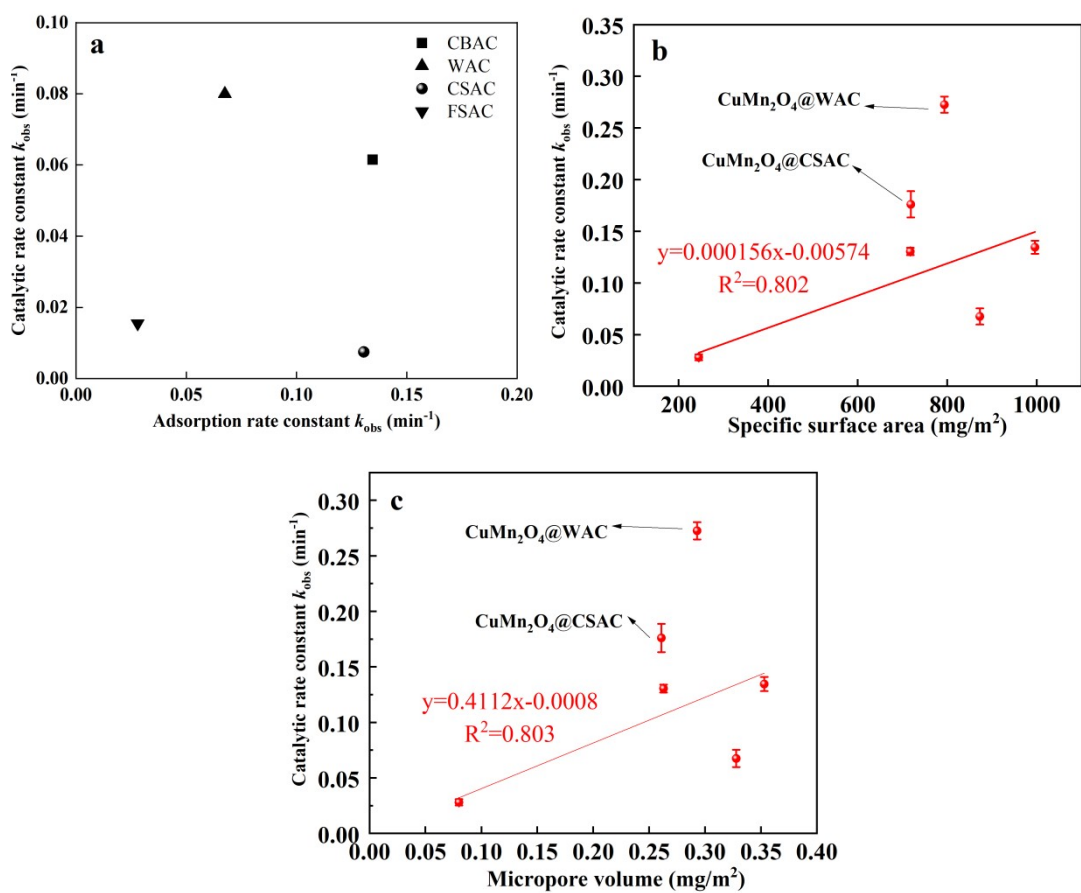


Fig. S11 Relationship between surface adsorption and observed reaction rate constant (k_{obs}) (a); Specific surface (b) and micropore volume (c) on k_{obs} in IBP degradation in the presence of AC or AC supported CuMn_2O_4 .

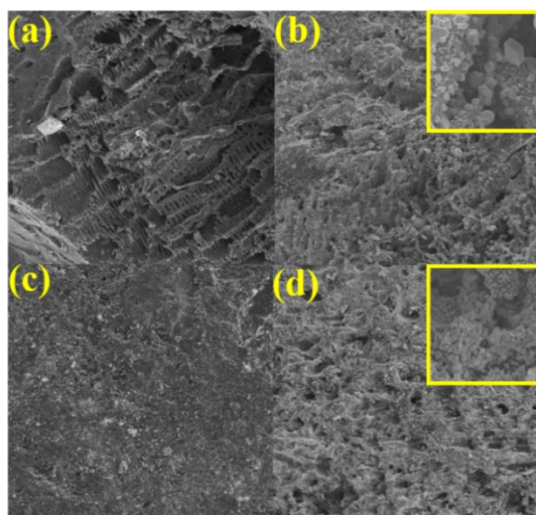


Fig. S12 SEM images of WAC (a) CuMn₂O₄@WAC (b) CSAC (c) and CuMn₂O₄@CSAC (d).

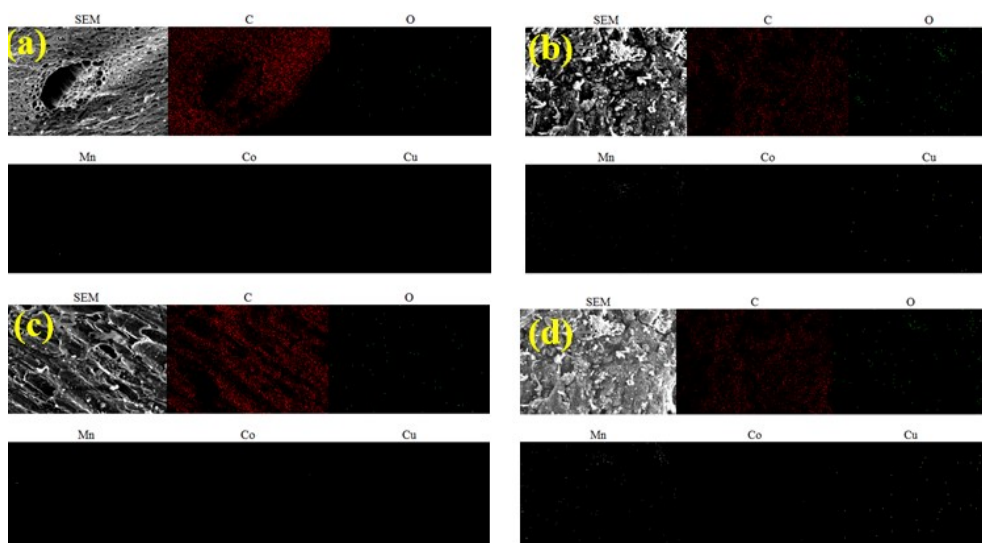


Fig. S13 EDS spectrum of WAC (a) CuMn₂O₄@WAC (b) CSAC (c) and CuMn₂O₄@CSAC (d).

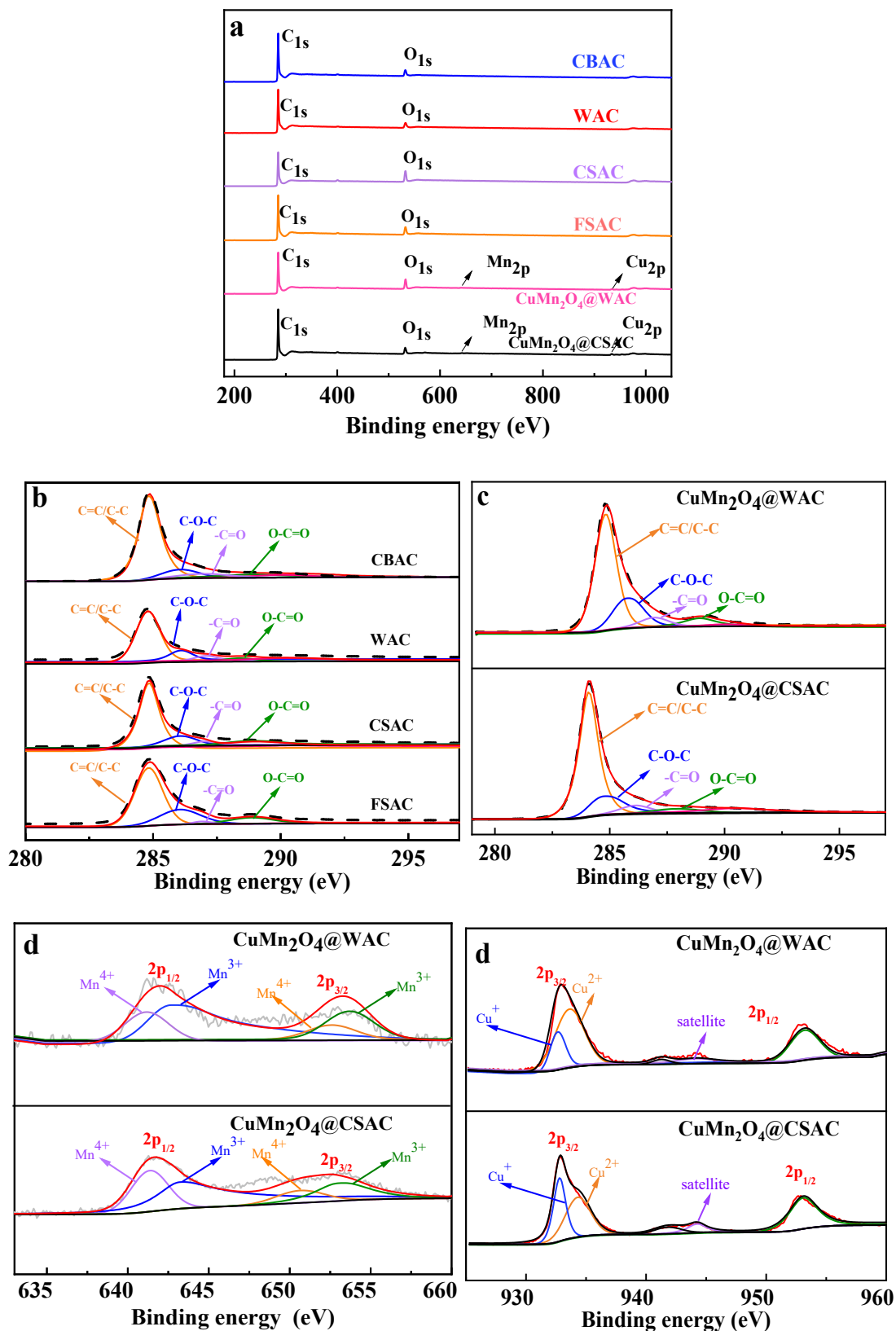


Fig. S14 XPS full spectrum of activated carbon and activated carbon supported CuMn_2O_4 (a) and XPS spectra of activated carbon-supported CuMn_2O_4 : (b) C 1s, (c)

Mn 2p, (d) Cu 2p (e).

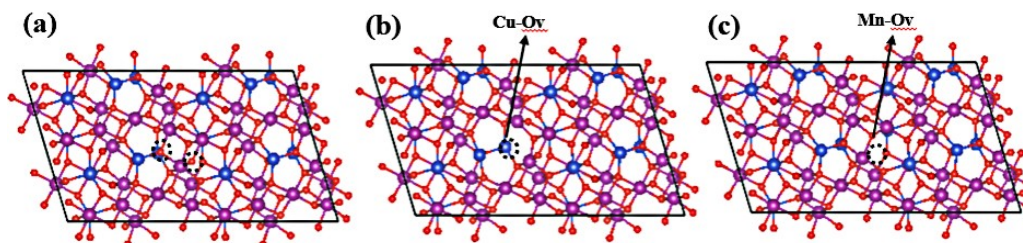


Fig. S15 The geometry structure of (a) pristine crystal plane (311), Mn-O_V plane (b) and Cu-O_V plane (c). Red: oxygen atom; Blue: copper atom, Purple: manganese atom.

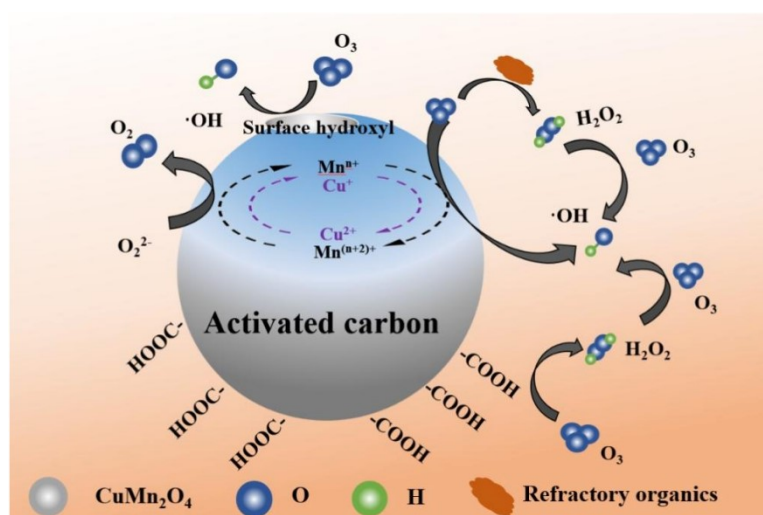


Fig. S16 Reaction mechanism of activated carbon supported CuMn₂O₄ catalytic ozonation of refractory organics in wastewater.

References

1. F. J. Benitez, L. A. Juan, J. R. Francisco, R. Gloria and R. Edgar Charry, Ozonation of benzotriazole and methylindole: Kinetic modeling, identification of intermediates and reaction mechanisms, *Journal of Hazardous Materials*, 2015, **282**, 224-232..
2. M. Panizza, A. Dirany, I. Sirés, M. Haidar, N. Oturan and M. A. Oturan, Complete mineralization of the antibiotic amoxicillin by electro-Fenton with a BDD anode, *Journal of Applied Electrochemistry*, 2014, **44**, 1327-1335.
3. Z. Song, M. Wang, Z. Wang, Y. Wang, R. Li, Y. Zhang, C. Liu, Y. Liu, B. Xu and F. Qi, Insights into Heteroatom-Doped Graphene for Catalytic Ozonation: Active Centers, Reactive Oxygen Species Evolution, and Catalytic Mechanism, *Environmental Science & Technology*, 2019, **53**, 5337-5348.
4. A. Ikhlaiq, D. R. Brown and B. Kasprzyk-Hordern, Mechanisms of catalytic ozonation: An investigation into superoxide ion radical and hydrogen peroxide formation during catalytic ozonation on alumina and zeolites in water, *Applied Catalysis B: Environmental*, 2013, **129**, 437-449.
5. I. Amir, R. C. Brown and K.-H. Barbara, Mechanisms of catalytic ozonation: An investigation into superoxide ion radical and hydrogen peroxide formation during catalytic ozonation on alumina and zeolites in water, *Applied Catalysis B-environmental*, 2013, **129**, 437-449.
6. Y. Renli, G. Wei, D. Jing, Z. Xiaoxia, H. Zheng, W. Qinglian, C. Jo-Shu and R. Nanqi, Heteroatoms doped graphene for catalytic ozonation of sulfamethoxazole by metal-free catalysis: Performances and mechanisms, *Chemical Engineering Journal*, 2017, **317**, 632-639.
7. N. K. Vel Leitner and B. Roshani, Kinetic of benzotriazole oxidation by ozone and hydroxyl radical, *Water Research*, 2010, **44**, 2058-2066.
8. M. Chys, W. T. M. Audenaert, E. Deniere, S. T. F. C. Mortier, H. Van Langenhove, I. Nopens, K. Demeestere and S. W. H. Van Hulle, Surrogate-Based Correlation Models in View of Real-Time Control of Ozonation of Secondary Treated Municipal Wastewater—Model Development and Dynamic Validation, *Environmental Science & Technology*, 2017, **51**, 14233-14243.
9. A. M. Chávez, F. J. Beltrán, J. López, F. J. Rivas and P. M. Alvarez, On the importance of reactions in the proximity of the gas-water interface: Application to direct ozone reactions of antibiotics in water, *Chemical Engineering Journal*, 2023, **458**, 141408.
10. M. C. Dodd, M. O. Buffle and U. Von Gunten, Oxidation of antibacterial molecules by aqueous ozone: Moiety-specific reaction kinetics and application to ozone-based wastewater treatment, *Environmental Science & Technology*, 2006, **40**, 1969-1977.
11. V. J. Pereira, H. S. Weinberg, K. G. Linden and P. C. Singer, UV Degradation Kinetics and Modeling of Pharmaceutical Compounds in Laboratory Grade and Surface Water via Direct and Indirect Photolysis at 254 nm, *Environmental Science & Technology*, 2007, **41**, 1682-1688.
12. M. M. Huber, S. Canonica, G. Y. Park and U. Von Gunten, Oxidation of pharmaceuticals during ozonation and advanced oxidation processes, *Environmental Science & Technology*, 2003, **37**, 1016-1024.
13. W.-L. Wang, Q.-Y. Wu, N. Huang, T. Wang and H.-Y. Hu, Synergistic effect between UV and chlorine (UV/chlorine) on the degradation of carbamazepine: Influence factors and radical species, *Water Research*, 2016, **98**, 190-198.
14. D. Gümüş and F. Akbal, A comparative study of ozonation, iron coated zeolite catalyzed ozonation and granular activated carbon catalyzed ozonation of humic acid, *Chemosphere*, 2017, **174**, 218-231.
15. J.-E. Lee, B.-S. Jin, S.-H. Cho, S.-H. Han, O.-S. Joo and K.-D. Jung, Catalytic ozonation of humic acids with Fe/MgO, *Reaction Kinetics and Catalysis Letters*, 2005, **85**, 65-71.
16. X. Chen, C. Wang, L. Jiang, H. Li, J. Wang and X. He, Pilot-scale catalytic ozonation pretreatment for improving the biodegradability of fixed-bed coal gasification wastewater, *Process Safety and Environmental Protection*, 2021, **148**, 13-19.
17. J. Xie, W. Chen, Y. Lv, H. Chen and L. Li, Synthesis of CeOx@SiO₂ with tandem effect

- of mass transfer and activation for enhancing sulfanilamide degradation with ozone, *Separation and Purification Technology*, 2021, **256**, 117823.
18. S. Shao, D. Lei, Y. Song, L. Liang and W. Jiao, Cu–MnO_x/γ-Al₂O₃ Catalyzed Ozonation of Nitrobenzene in a High-Gravity Rotating Packed Bed, *Industrial & Engineering Chemistry Research*, 2021, **60**, 2123-2135.
 19. H. Jiang, R. Zhang, J. Hao, X. Xu and F. Yang, Design, preparation, characterization, and application of Mn_xCu_{1-x}O_y/γ-Al₂O₃ catalysts in ozonation to achieve simultaneous organic carbon and nitrogen removal in pyridine wastewater, *Science of The Total Environment*, 2021, **774**, 145189.
 20. W. Jiao, X. Wei, S. Shao and Y. Liu, Catalytic decomposition and mass transfer of aqueous ozone promoted by Fe-Mn-Cu/γ-Al₂O₃ in a rotating packed bed, *Chinese Journal of Chemical Engineering*, 2021, **45**, 133-142.
 21. D. Liu, C. Wang, Z. Wang, Y. Sun, X. Liu, S. Xiao, L. Li and J. Zhou, Magnetically separable NiFe₂O₄/sepiolite catalyst for enhanced ozonation treatment of quinoline and bio-treated coking wastewater in a catalytic ozonation system, *Process Safety and Environmental Protection*, 2022, **159**, 422-432.
 22. Y.-C. Yang, Shang-ShengOuyang, YiSang, LeYang, Shi-YingZhang, Xue-QinHuang, Ya-YanYe, JingXiao, Mei-TianZhang, Na, An intensified ozonation system in a tank reactor with foam block stirrer: Synthetic textile wastewater treatment and mass transfer modeling, *Separation and Purification Technology*, 2021, **257**, 117909.
 23. H. Liu, Y. Gao, J. Wang, J. Pan, B. Gao and Q. Yue, Catalytic ozonation performance and mechanism of Mn-CeO_x@γ-Al₂O₃/O₃ in the treatment of sulfate-containing hypersaline antibiotic wastewater, *Science of The Total Environment*, 2022, **807**, 150867.
 24. W. Yang, B. Vogler, Y. Lei and T. Wu, Metallic ion leaching from heterogeneous catalysts: an overlooked effect in the study of catalytic ozonation processes, *Environmental Science Water Research & Technology*, 2017, **3**, 1143-1151.
 25. M. Shiraga, T. Kawabata, D. Li, T. Shishido, K. Komaguchi, T. Sano and K. Takehira, Memory effect-enhanced catalytic ozonation of aqueous phenol and oxalic acid over supported Cu catalysts derived from hydrotalcite, *Applied Clay Science*, 2006, **33**, 247-259.
 26. Y. Yang, X. Shi, M. Zhao, S. Chu and J. Xiao, Heterogeneous Catalytic Ozonation of Phenol by a Novel Binary Catalyst of Fe-Ni/MAC, *Catalysts*, 2020, **10**, 1123.
 27. C. Shan, Y. Xu, M. Hua, M. Gu, Z. Yang, P. Wang, Z. Lu, W. Zhang and B. Pan, Mesoporous Ce-Ti-Zr Ternary Oxide Millispheres for Efficient Catalytic Ozonation in Bubble Column, *Chemical Engineering Journal*, 2018, **338**, 261-270.
 28. A. S. Fajardo, R. C. Martins and R. M. Quinta-Ferreira, Treatment of a simulated phenolic effluent by heterogeneous catalytic ozonation using Pt/Al₂O₃, *Environmental Technology*, 2013, **34**, 301-311.
 29. S. S. Sable, F. Medina and S. Contreras, Clofibrac acid degradation by catalytic ozonation using hydrotalcite-derived catalysts, *Applied Catalysis B-Environmental*, 2014, **150**, 30-36.
 30. S. S. Sable, F. Medina and S. Contreras, Clofibrac acid degradation by catalytic ozonation using hydrotalcite-derived catalysts, *Applied Catalysis B: Environmental*, 2014, **150**, 30-36.